

Cold atomic collisions studied by molecular spectroscopy

C. Samuelis,¹ E. Tiesinga,² T. Laue,¹ M. Elbs,¹ H. Knöckel,¹ and E. Tiemann¹¹*Institut für Quantenoptik, Universität Hannover, 30167 Hannover, Germany*²*Atomic Physics Division, National Institute of Standards and Technology, Gaithersburg, Maryland 20899*

(Received 20 July 2000; published 12 December 2000)

We observe bound states just below the dissociation limit and shape and Feshbach resonances between the ground state hyperfine asymptotes by Raman spectroscopy on a molecular beam of sodium dimers. The rotational selectivity of a two-photon transition gives access to specific states of nuclear motion and thus to cold collision properties of two colliding atoms. Modeling of the collisional resonance structures requires a multichannel treatment of the nuclear dynamics that uses highly accurate $X^1\Sigma_g^+$ and $a^3\Sigma_u^+$ potentials. These potentials are constructed from bound levels just below the ground state asymptote measured in this experiment and bound state information available in the literature. We also present simulations of the spectrum between the ground state hyperfine asymptotes. The good agreement shows that accurate potentials obtained from bound state information are able to reproduce scattering properties of two colliding sodium atoms. From this analysis we find for the scattering lengths $a(f=2) = a_{1,-1} = 52.98(40)a_0$, $a_{\text{singlet}} = 19.20(30)a_0$, and $a_{\text{triplet}} = 62.51(50)a_0$, where $1a_0 = 0.0529177$ nm.

DOI: 10.1103/PhysRevA.63.012710

PACS number(s): 34.20.Cf, 34.50.-s

I. INTRODUCTION

Due to the fast progress in cooling and trapping cold atoms during recent years, the interest in detailed knowledge of two-particle interactions that are able to reproduce ultracold collision properties has increased. At ultracold temperatures these interactions are determined by the scattering lengths and long range attraction of the interaction potentials. The scattering length, which is derived from the scattering wave function at zero collision energy, determines the effectiveness of evaporative cooling and the stability of Bose-Einstein condensates [1,2]. It can be derived from a variety of experiments. Photoassociation [3] with ultracold atoms in a magneto-optical trap can determine the last nodal positions of the zero energy collisional wave function. Alternatively, the scattering length can be determined from the energy position of the last bound state with respect to the dissociation limit [4]. In both cases the experimental observables are converted into the scattering length by relying on the accurate van der Waals coefficient C_6 , which has been obtained from atomic properties.

Recently, different derivations of such potentials for Na_2 at the ground state asymptote $3s+3s$ have been published. The approach by Ho *et al.* [5] uses experimental data up to vibrational levels $v_X=62$ of $X^1\Sigma_g^+$ and for $a^3\Sigma_u^+$ only data with minor accuracy compared to the singlet, resulting in a potential that will be not sufficient for the precise description of cold collisions. The method by van Abeelen *et al.* [6] concentrates on the long range behavior and describes the short range by the accumulated phase from a small up to an appropriately chosen internuclear separation ($R_0=16$ Å in their case). They use almost the same set of data as Ho [5] but include the recent measurements of Feshbach resonances at zero collision energy in a magnetic field studied by Inouye *et al.* [7] to get the right asymptotic behavior for cold collisions.

A more fundamental approach of obtaining scattering properties for sodium dimers becomes possible due to the measurements presented in this paper. We will show that

Raman spectroscopy on a molecular sodium beam selectively accesses weakly bound states just below the ground state dissociation limit as well as scattering resonances between the hyperfine asymptotes. The data set of bound states has now become sufficiently complete to derive highly accurate singlet $X^1\Sigma_g^+$ and triplet $a^3\Sigma_u^+$ potential surfaces. These potentials are valid not only for large internuclear separations but also for internuclear separations down to the repulsive branch of the surfaces.

For the extraction of the singlet/triplet Born-Oppenheimer (BO) potentials we have set up a multichannel description of the vibrational-rotational motion. The atomic hyperfine interaction of the individual sodium atoms mixes the $X^1\Sigma_g^+$ and $a^3\Sigma_u^+$ potentials. This multichannel description is also valid for atom-atom scattering and enables us not only to determine scattering lengths but also to describe collisions well above the dissociation limit and to give an interpretation for the observed resonance structures in terms of shape and Feshbach resonances.

The paper is set up as follows. In Sec. II we briefly describe the experiment, focusing on how Raman spectroscopy selectively addresses single rotational levels. This section also presents the energies of asymptotic bound states and resonances. Section III describes how approximate Born-Oppenheimer potentials are extracted. In Sec. IV an outline of the multichannel Hamiltonian is given. The multichannel bound state solutions of this Hamiltonian are used for final adjustments of the BO potentials. Section V sets up the multichannel scattering theory and the description of the optical transition to model the resonances in the spectra between the hyperfine asymptotes. A comparison of the experimental results and the theoretical model is given in Sec. VI. We end with a section that compares the present results to earlier findings and gives perspectives for further studies.

II. EXPERIMENT

We will briefly review the experimental setup. Details are published in Ref. [8]. From an appropriately chosen vibra-

tionally excited level v_X in the ground state with a Raman transition via the intermediate level (A, v'_A, J'_A) , levels at the ground state asymptote $3s + 3s$ of Na_2 are observed.

In a first interaction zone, for preparing the above mentioned level v_X a dye laser $L1$ (at 610 nm) intersects perpendicularly with a well collimated molecular beam. In the laser beam some of the molecules undergo a Franck-Condon pumping step. Molecules that are initially in the lowest vibrational level of the $X^1\Sigma_g^+$ state are transferred to the $v_X \approx 30$ vibrational levels of the X state by absorbing an $L1$ photon to a low lying A state vibrational level and a subsequent spontaneous emission.

In a second interaction zone separated by 35 cm from the first the ground state asymptote is reached in a STIRAP-like (stimulated Raman scattering involving adiabatic passage) process [9] starting from a single rovibrational level $v_X \approx 30$, J_X . The STIRAP pulse sequence is applied by two cw laser beams, $L2$ and $L3$ (at 530 nm and 590 nm), partially overlapping in space and perpendicular to the molecular beam. The polarization of the two lasers is linear and parallel to each other and to the molecular beam.

Fluorescence from the intermediate level (A, v'_A, J'_A) populated by laser $L2$, which is kept at fixed frequency, is monitored with a photomultiplier. This fluorescence decreases when the tunable laser $L3$ comes in resonance with the intermediate level and an asymptotic ground state level. The resulting dip in the fluorescence can be up to 70% for strong signals. The narrow linewidths down to 20 MHz are not determined by the lifetime of the intermediate state, but by residual Doppler broadening from angular misalignment of the $L2$ and $L3$ lasers, by saturation broadening, and by Zeeman broadening due to residual magnetic fields. The frequencies of the asymptotic ground state levels are calibrated with a temperature stabilized 150 MHz marker cavity. This allows the determination of the difference frequencies with respect to well calibrated ‘‘singlet’’ lines [8] with an uncertainty of less than 10 MHz.

The initial and intermediate states of the STIRAP transition determine the accessible states near the ground state asymptotes $\text{Na}(^2S_{1/2}, f_a) + \text{Na}(^2S_{1/2}, f_b)$, where f_a and f_b are the total angular momenta (electron and nuclear spin) of atoms a and b , respectively. Two ground state sodium atoms $\text{Na}(^2S_{1/2}, f_a) + \text{Na}(^2S_{1/2}, f_b)$ can combine to three different molecular asymptotes characterized by $f_a + f_b = 1 + 1$, $1 + 2$, and $2 + 2$.

The intermediate state is a rovibrational level v'_A, J'_A of the $A^1\Sigma_u^+$ potential. The selection rules for absorption of our linearly polarized photon require that $J'_A = J_X \pm 1$. Moreover, as a consequence of the nonzero electronic mechanical angular momentum of the A state, even (odd) J'_A levels contain a combination of odd (even) partial waves l . In fact, for $J'_A = 0$ only $l = 1$ partial waves contribute while for $J'_A = 1$ the molecular wave function is a linear combination of $l = 0$ and $l = 2$ partial waves. For $J'_A = 2$ and $J'_A = 3$ we have $l = 1, 3$ and $l = 2, 4$, respectively.

Unlike in the intermediate A state level, the partial wave l for two interacting 2S atoms is a good quantum number. Consequently, the values of l of the weakly bound ground

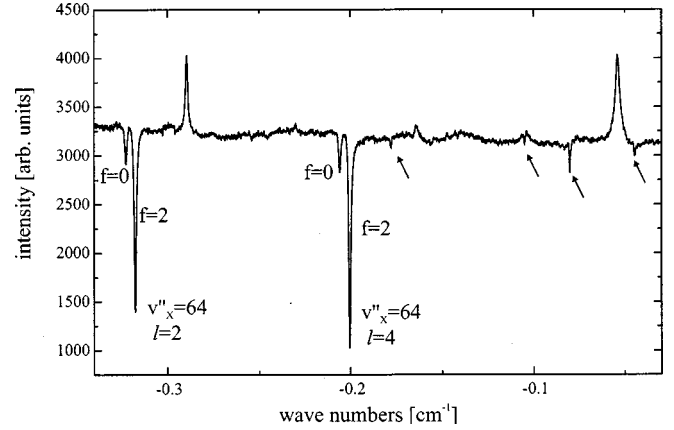


FIG. 1. A spectrum using the $v'_A = 120$, $J'_A = 3$ rovibrational A state as the intermediate state. Selection rules ensure that only even l bound states are observable. The $v''_X = 64$ $X^1\Sigma_g^+$ levels are labeled by l, f and the four $a^3\Sigma_u^+$ lines are marked with arrows. The zero of energy is the $\text{Na}(f_a = 1) + \text{Na}(f_b = 1)$ dissociation limit.

state levels which can be accessed by stimulated emission from a J'_A intermediate level are limited. For example, for an intermediate $J'_A = 1$ level $s(l = 0)$ - and $d(l = 2)$ -wave bound levels below, or corresponding partial waves between and above the dissociation limits can be observed.

Near the ground state asymptotes, the $X^1\Sigma_g^+$ and $a^3\Sigma_u^+$ potentials are strongly mixed by the hyperfine interaction. In the absence of this mixing the stimulated downward transition could access only the $X^1\Sigma_g^+$ levels as dipole selection rules require $u \rightarrow g$ transitions. Near the dissociation limits $a^3\Sigma_u^+$ levels become accessible due to hyperfine mixing with $X^1\Sigma_g^+$ levels. The mixing can be so strong that labeling as singlet and triplet is inappropriate. We expect very strong signals to levels that are almost pure singlet levels and weak signals for triplet levels that couple to the singlet manifold. In Sec. IV we discuss the good quantum numbers for two interacting ground state atoms in more detail.

We have measured almost all lines or resonances with $l \leq 5$ covering an energy region from 0.36 cm^{-1} below the $f_a = 1 + f_b = 1$ asymptote up to the $f_a = 2 + f_b = 2$ asymptote. The strong lines with large $X^1\Sigma_g^+$ character were already observed in [8]. The weaker resonances with high $a^3\Sigma_u^+$ character are observable only by carefully choosing the intermediate vibrational level to ensure a maximum Franck-Condon overlap. For the $v''_a = 14$ and 15 vibrational levels of the $a^3\Sigma_u^+$ state, $v'_A = 120$ and 140 of the A state have been used, respectively. To increase the signal-to-noise ratio several scans are averaged giving a typical total recording time of 30 min for a complete spectrum. In addition, the intensity of $L3$ is increased up to 100 W/cm^2 . The enhanced uncertainty in the frequency determination of weak lines, due to power broadening of the strong singlet lines used as reference, is below 5 MHz.

An example of a spectrum that shows weakly bound $X^1\Sigma_g^+$ and $a^3\Sigma_u^+$ levels is presented in Fig. 1. The figure shows the Raman spectrum tuning laser $L3$. The initial state is the $v_X = 29$, $J_X = 4$ $X^1\Sigma_g^+$ rovibrational level and the intermediate state is the $v'_A = 120$, $J'_A = 3$ of the A state. The

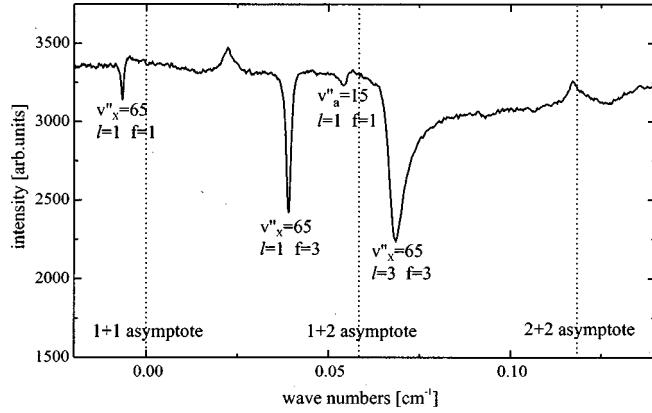


FIG. 2. A spectrum using the $v'_A=140$, $J'_A=2$ rovibrational A state as the intermediate state. The dotted lines indicate the three hyperfine dissociation limits f_a+f_b . Selection rules ensure that only odd l bound states or resonances are observable.

weakly bound ground state levels appear as dips in the fluorescence spectrum. Two spectral features with increased fluorescence are due to accidental excitations of $A-X$ lines by scanning laser $L3$ and are not related to laser $L2$. If one chooses a different intermediate level v'_A these lines will disappear and enhanced fluorescence might occur at other accidental frequencies. In this way undesired overlaps between fluorescence peaks and dips can be avoided.

Dipole selection rules ensure that only $l=2$ and 4 lines can be observed in Fig. 1. The strong doublets are hyperfine structures of the $v''_X=64$, $l=2,4$ rovibrational levels of $X^1\Sigma_g^+$. These two components can be labeled by the good quantum number f from $\vec{f}=\vec{f}_a+\vec{f}_b$. The features marked by arrows are levels that predominantly have $a^3\Sigma_u^+$ character. Assignment of the weakly bound $X^1\Sigma_g^+$ levels is from Ref. [8].

In Fig. 2 we present an example of a STIRAP spectrum spanning the three $\text{Na}(f_a)+\text{Na}(f_b)$ hyperfine dissociation limits, which are indicated by the three dotted lines. The initial state is the $v_X=29$, $J_X=3$ $X^1\Sigma_g^+$ rovibrational level

and the intermediate state is $v'_A=140$, $J'_A=2$ of the A state. Hence selection rules ensure that only odd l features are observed. The dip below the energetically lowest $\text{Na}(f_a=1)+\text{Na}(f_b=1)$ limit is a true bound state. Other features in Fig. 2 except the upward peaks are scattering resonances. Their assignment is discussed in detail in later sections. Here it is worth noting that labeling with $X^1\Sigma_g^+$ vibrational quantum numbers v''_X is only approximate. In reality, mixing with the $a^3\Sigma_u^+$ state is so strong that an analysis using the $X^1\Sigma_g^+$ state alone is insufficient.

A list of our experimental line positions and their uncertainties with respect to the lowest dissociation asymptote is presented in Tables I and II. The uncertainties are determined by different calibration steps for the intermediate levels used. Details are given in [8]. The accuracy of some of the lower levels reported in Ref. [8] has been improved by wide scans spanning a large asymptotic energy range including the well calibrated last vibrational levels.

III. GROUND-STATE POTENTIALS

A theoretical interpretation of the observed level structure of the last vibrational levels of the $X^1\Sigma_g^+$ state with a model based on adiabatic electronic potentials was tested in [8]. Unfortunately, the theoretical predictions for the hyperfine structure are not in agreement with the observed splittings. Nonadiabatic effects are not negligible for the description of the asymptotic level structure. A coupled channel analysis including hyperfine coupling between singlet and triplet states is necessary to model the asymptotic region. For the theoretical approach used in this paper, potentials are needed describing the molecule at small internuclear distances and applicable as Born-Oppenheimer potentials in the asymptotic region. To construct them we use data from the literature for the lower part of the $X^1\Sigma_g^+$ and $a^3\Sigma_u^+$ potentials together with our own asymptotic measurements. In the low part of the potentials we can start with a single channel model because the hyperfine coupling is small compared to the level spacing.

TABLE I. Level energies (in cm^{-1}) for even l with respect to the dissociation limit $3s(f_a=1)+3s(f_b=1)$, which is at $5942.6148(39)$ cm^{-1} [8] with respect to $v_X=0$, $J_X=0$. f_a, f_b are approximate assignments, the good quantum number is f ($\vec{f}=\vec{f}_a+\vec{f}_b$). The numbers in parentheses represent 1σ uncertainties of the bound state and resonance positions. S is a shape resonance, F a Feshbach resonance, and * indicates values used in the fit of Sec. IV.

l	f	v''_X	$(f_a, f_b)=(1,1)$	v''_a	$(f_a, f_b)=(1,2)$	v''_a	$(f_a, f_b)=(2,2)$
2	2	65		15	+0.0584(9) F		
	0,2		+0.0024(9) S				
0	2	65	-0.0106(7)*	15	+0.0416(9) F		
	0		-0.0131(7)*				
4	2	64	-0.2007(12)*	14	-0.0808(12)*	14	-0.0090(12)*
	0		-0.2063(12)*				-0.0452(12)*
2	2		-0.3177(9)*		-0.1782(12)*		-0.1056(12)*
	0		-0.3227(9)*				-0.1423(12)*
0	2		-0.3696(9)*		-0.2221(12)*		-0.1494(12)*
	0		-0.3744(9)*				-0.1860(13)*

TABLE II. Level energies (in cm^{-1}) for odd l with respect to the dissociation limit $3s(f_a=1)+3s(f_b=1)$, which is at $5942.6148(39) \text{ cm}^{-1}$ [8] with respect to $v_X=0, J_X=0$. S is a shape resonance, F a Feshbach resonance, and * indicates values used in the fit of Sec. IV.

l	f	v_X''	$(f_a, f_b)=(1,1)$	v_X''	$(f_a, f_b)=(1,2)$	v_a''	$(f_a, f_b)=(1,2)$	v_a''	$(f_a, f_b)=(2,2)$
3	3	65		65	+0.0679(11) S^*	15			
1	3				+0.0384(9)*				
	1		-0.0065(9)*				+0.0537(12) F		
5	3	64		64	-0.1134(14)*	14		14	
	1		-0.1253(14)*				-0.0003(14)*		+0.0392(14) F
3	3				-0.2608(14)*				-0.0501(17)*
	1		-0.2707(14)*				-0.1186(14)*		-0.0783(17)*
1	3				-0.3467(17)*				-0.1223(20)*
	1		-0.3554(17)*				-0.1911(17)*		

For vibrational levels $v_X = 0$ up to 45 of the $X^1\Sigma_g^+$ state, we take the parameters of analysis 2 of Ref. [10] and, because no primary spectral data are available to us, we calculate energies for levels from $v_X=0$ to 45 with selected rotational quantum number J_X between 0 and 100. For $46 \leq v_X \leq 62$ the level energies reported by Barrow *et al.* [11] are used, but corrected for the small shift $\Delta E = -0.0180 \text{ cm}^{-1}$ due to the recalibration [8] of their reference level. For low angular momenta of $v_X=61$ to 63 our own measurements [8] are included. $v_X=64$ and 65 are excluded because they are disturbed by the coupling between X and a states. First a Rydberg-Klein-Rees (RKR) potential is derived from the above data. This RKR potential is then represented analytically by a power series:

$$V(R) = -D + a_0 + a_1\xi + a_2\xi^2 + a_3\xi^3 + \dots \quad (1)$$

with

$$\xi = \xi(R, b) = \frac{R - R_e}{R + bR_e}, \quad (2)$$

where R_e is the equilibrium internuclear separation of the initial RKR potential and the parameters b, a_0, a_1 , etc. are determined from a least squares fit procedure of the RKR potential. The parameter b in Eq. (2) models the very different steepness of the potential inside and outside R_e and is chosen such that the number of a_i coefficients needed to represent the RKR potential is minimal. D is the energy difference of $V(R=R_e)$ of the $X^1\Sigma_g^+$ ground state and the energy of the barycenter of the hyperfine structure at the asymptote. Thus we shift the zero of energy to the barycenter of the hyperfine structure in order to have a common reference for all parts of the potential.

The parameters a_i are refined by minimizing the differences between the experimental energy levels and those numerically calculated using a Numerov method for finding the bound states of a Schrödinger equation. The linear term a_1 in Eq. (1) is needed, because the equilibrium separation of the exact potential is not necessarily equal to that of the RKR potential. The shift of the minimum is very small as can be estimated from $|a_1| \ll |a_2|$. The result of the fit is given in Table III.

For the calculations near the dissociation limit the potential must be extended to smaller and larger internuclear separations than can be obtained in the above fit. For ($R \leq R_i = 2.24 \text{ \AA}$) we use the exponential form

$$V_i(R) = A_i e^{-B_i(R-R_i)} - D. \quad (3)$$

The coefficients A_i and B_i (see Table III) are fixed by the condition that the connection at R_i is continuous and differentiable. For ($R \geq R_o = 9 \text{ \AA}$) the potential is written as

$$V_o(R) = -\frac{C_6}{R^6} - \frac{C_8}{R^8} - \frac{C_{10}}{R^{10}} - \frac{C_{12}}{R^{12}} - \frac{C_{14}}{R^{14}} + E_{ex}(R) \quad (4)$$

with

$$E_{ex}(R) = -A_{ex} R^\gamma e^{-B_{ex}R} \quad (5)$$

for the exchange interaction. The terms C_{12} and C_{14} are used only to guarantee a smooth connection at R_o . The values of the coefficients are given in Tables III and IV.

The description of the potential for the $a^3\Sigma_u^+$ state is quite similar to that of the singlet. A RKR potential for $v_a = 0-12$ is given by Li *et al.* [12]. This potential is converted to the analytic form of Eq. (1). Starting from this fit the values of a_i are improved by minimizing the differences between the theoretical level energies and the experimental level energies from [12] and our values for $v_a = 14$ (see Tables I and II). In order to obtain a reliable potential near the equilibrium internuclear separation the rotational constant for $v_a=0$ from [13] is included in the fit as well. For $R > R_o = 9 \text{ \AA}$, the long range tail of the potential is given by Eq. (4) except that the exchange interaction is of opposite sign. C_{12} and C_{14} are again determined by smooth connection at R_o . The repulsive branch of the triplet potential ends at much larger separations than that of the singlet potential. For $R < R_i = 4.4 \text{ \AA}$ the exponential representation is given by Eq. (3). The a_i and other coefficients of the triplet potential are given in Table V.

It should be noted that the accuracies of binding energies of the low lying vibrational levels of the $X^1\Sigma_g^+$ and $a^3\Sigma_u^+$ potentials are 0.01 cm^{-1} and 0.5 cm^{-1} , respectively. The

TABLE III. Parameters used for the $X^1\Sigma_g^+$ potential. The dimension of a_i is cm^{-1} . The b parameter is dimensionless. The dimension of length is the angstrom where $1 \text{ \AA} = 0.1 \text{ nm}$. In order to faithfully represent the potentials, coefficients are given to 18 significant figures. This does not reflect the accuracy of the potentials in reproducing experimental energies. Numbers in square brackets are powers of 10.

R_e	3.07857466 \AA	R_i	2.24 \AA	R_o	9.00 \AA
b	-0.4	A_i	0.503512346[04] cm^{-1}	C_{12}	0.400101 4[12] $\text{cm}^{-1} \text{\AA}^{12}$
D	6022.03976[00] cm^{-1}	B_i	0.29139632[01] \AA^{-1}	C_{14}	-0.3773101[14] $\text{cm}^{-1} \text{\AA}^{14}$
a_0	0.0000000000[00]	a_1	-0.100366956846468103[01]	a_2	0.147293394381249527[05]
a_3	0.121449677360197838[05]	a_4	0.940840875482991805[03]	a_5	-0.989168749563361598[04]
a_6	-0.893669291900001190[04]	a_7	-0.276220838436417398[05]	a_8	-0.255644809410814487[06]
a_9	0.226159933011279383[06]	a_{10}	0.538844461650854349[07]	a_{11}	-0.510577439684730303[07]
a_{12}	-0.964362923547747433[08]	a_{13}	0.397842889234429672[08]	a_{14}	0.120638159409995508[10]
a_{15}	0.135115832858087450[09]	a_{16}	-0.105481785684501114[11]	a_{17}	-0.577602571758915329[10]
a_{18}	0.655110694986436462[11]	a_{19}	0.601611120985334625[11]	a_{20}	-0.291981622040804688[12]
a_{21}	-0.369890125460666565[12]	a_{22}	0.931341683721645020[12]	a_{23}	0.153825346767959692[13]
a_{24}	-0.207002754418455908[13]	a_{25}	-0.452860991461020020[13]	a_{26}	0.293752239182879736[13]
a_{27}	0.955650226916233398[13]	a_{28}	-0.176550075860125781[13]	a_{29}	-0.143185459101196270[14]
a_{30}	-0.222433768486321191[13]	a_{31}	0.147122134848085840[14]	a_{32}	0.640989986244799219[13]
a_{33}	-0.955519484939274023[13]	a_{34}	-0.688834959288581738[13]	a_{35}	0.312161800940854639[13]
a_{36}	0.377637982042295654[13]	a_{37}	0.242656911184852371[11]	a_{38}	-0.872613116275821289[12]
a_{39}	-0.236755792281878265[12]				

latter uncertainties are significantly larger because of the limited accuracy of the existing data [10–12].

IV. COUPLED CHANNELS DESCRIPTION OF THE GROUND-STATE SODIUM DIMER

The structure of the Hamiltonian that can quantitatively describe the molecular dynamics of a ground state sodium dimer or two colliding 2S sodium atoms is well known. It has, for example, been elegantly discussed in Refs. [14,15]. Briefly, the Hamiltonian contains the kinetic energy operator for the relative radial motion between two atoms, the two Born-Oppenheimer potentials, a hyperfine contact interaction for each Na atom, and the nuclear rotation $\hbar^2 \hat{I}^2 / (2\mu R^2)$ where μ is the reduced mass. Weak magnetic spin-spin and second-order spin-orbit interactions can be neglected for the purpose of this paper. These interactions become important when the accuracy in the determination of the position of weakly bound levels reaches a few megahertz. The atomic mass and atomic hyperfine constant that are applied can be found in Refs. [16] and [17], respectively. The nuclear spin of a sodium atom is $3/2$.

For the ground-state Na dimer the nuclear orbital angular momentum \vec{l} , the total atomic spin $\vec{f} = \vec{f}_a + \vec{f}_b$, and the total angular momentum of the molecule $\vec{F} = \vec{l} + \vec{f}$ are conserved.

TABLE IV. Long range dispersion coefficients and exchange interaction parameters used for both $X^1\Sigma_g^+$ and $a^3\Sigma_u^+$ potentials. $A_{ex}R^\gamma$ and R are in units of cm^{-1} and \AA , respectively [20–22]. Numbers in square brackets are powers of 10.

C_6	0.7523052[07] $\text{cm}^{-1} \text{\AA}^6$	C_8	0.1509850[09] $\text{cm}^{-1} \text{\AA}^8$
C_{10}	0.4181980[10] $\text{cm}^{-1} \text{\AA}^{10}$	γ	5.504
A_{ex}	8690.0	B_{ex}	2.3250 \AA^{-1}

Two basis sets are now convenient for understanding the couplings contained in the Hamiltonian. These are the atomic $|(f_a f_b) f I F\rangle$ and molecular $|(S I) f I F\rangle$ bases, where $\vec{f} = \vec{S} + \vec{I}$ and S is the total electron spin and I is the total nuclear spin. The Na atoms are composite bosons and consequently roughly one-half of the possible angular momentum states can exist in the dimer. This reduction of allowed spin states is most concisely expressed by the requirement that $S + I + l$ is even in the molecular basis. A transformation between the two basis sets is obtained using angular momentum recoupling theory. The Hamiltonian in these equivalent basis sets gives rise to a set of close coupled or coupled channels equations. For example for $l=0$, $f=F=2$ the three atomic states $|(f_a f_b)\rangle = |(11)\rangle$, $|(12)\rangle$, and $|(22)\rangle$ are coupled.

In this paper we are interested in both continuum and bound state solutions of the coupled channels equations. A discussion of the continuum solutions is postponed to Sec. V. For the bound states of the Hamiltonian it is convenient to discretize the kinetic energy operator using a Fourier grid representation that automatically ensures that wave functions are zero at the smallest and largest internuclear separations included in the discretization [18]. The Fourier grid method is simple to implement and is able with a minimum of collocation points to represent the bound states with a high degree of accuracy. Finding the bound states is reduced to solving a matrix eigenvalue problem.

An approximation of the Hamiltonian based on the relative strength of the interactions has been fruitfully used in the previous section. In fact, the hyperfine interaction has been neglected. The validity of this approximation can be understood from the quantum numbers of the two basis sets. The Born-Oppenheimer surfaces, which describe states of total electron spin $S=0$ or 1, are diagonal in the molecular basis. On the other hand the atomic hyperfine interactions have a diagonal representation in the atomic basis. It there-

TABLE V. Parameters used for the $a^3\Sigma_u^+$ potential. The dimension of a_i is cm^{-1} . The b parameter is dimensionless. Numbers in square brackets are powers of 10.

R_e	5.09110000 Å	R_i	4.40 Å	R_o	9.00 Å
b	-0.2	A_i	0.594159163[04] cm^{-1}	C_{12}	-0.4122657[13] cm^{-1} Å ¹²
D	6022.03976[00] cm^{-1}	B_i	0.51920509[-01] Å ⁻¹	C_{14}	0.3189688[15] cm^{-1} Å ¹⁴
a_0	5849.33285580000000[00]	a_1	-0.643826131719923609[02]	a_2	0.177313825420407102[04]
a_3	-0.405570252514369685[02]	a_4	-0.409898389855788628[04]	a_5	-0.189373310208704679[05]
a_6	0.608731652094501042[05]	a_7	-0.449581549142197837[05]		

fore follows that the hyperfine interactions couple the $X^1\Sigma_g^+$ and $a^3\Sigma_u^+$ states in the molecular basis while the BO potentials mix the atomic hyperfine states in the atomic basis. The rotational part of the Hamiltonian is diagonal in both basis sets.

The structure of the Hamiltonian suggests that a change from a predominantly molecular to an atomic representation occurs as a function of binding energy. For large binding energies the splitting of the BO potentials is much larger than hyperfine splittings. The approximation used in the previous section is then valid and single channel bound state calculations are sufficient to invert the experimental level positions into either the $X^1\Sigma_g^+$ or $a^3\Sigma_u^+$ potentials. For smaller binding energies hyperfine splittings are larger than the exchange splitting between the $X^1\Sigma_g^+$ and $a^3\Sigma_u^+$ potentials and the full coupled channels eigenvalue problem needs to be solved. It turns out that for the sodium dimer the single channel approximation is valid for levels that are bound by more than $\approx 1 \text{ cm}^{-1}$.

An adiabatic approximation has been used to assign the experimentally observed weakly bound levels of Ref. [8] as well as those presented in Tables I and II. In essence for a given lF the interactions are diagonalized at each internuclear separation. The R -dependent eigenvalues or adiabats closely follow the $X^1\Sigma_g^+$ or $a^3\Sigma_u^+$ potential for short internuclear separation and asymptotically dissociate to one of the three f_a+f_b limits. In fact, for even l the adiabat that at short range is nearly the $X^1\Sigma_g^+$ state dissociates to the $f_a=1+f_b=1$ limit. The levels of the two tables are assigned by lf , the dissociation limit, and the vibrational quantum number of the corresponding adiabat. The energies are independent of the total molecular spin F , because we neglect electron spin-spin and second-order spin-orbit interaction, and hence F is not needed to label the levels.

The assignment of levels by adiabats is used for convenience but the labeling by adiabat and vibrational quantum number is only approximate and the lf labels can only be confirmed with a coupled channels calculation. In fact, the difference between eigenenergies of an adiabatic and a coupled channels calculation can be on the order of the hyperfine splitting.

One way of investigating the effects of close coupling is for each multichannel eigenfunction to look at expectation values of spin operators such as \hat{S}^2 or \hat{f}_a^2 and \hat{f}_b^2 [18]. If an eigenfunction contains significant $S=0$ character, as might be true for deeply bound levels, the expectation value of \hat{S}^2 is nearly zero and the eigenstate can be labeled by $X^1\Sigma_g^+$

and the three conserved quantum numbers f_lF . On the other hand, mixing between the $X^1\Sigma_g^+$ and $a^3\Sigma_u^+$ states shows up as expectation values of \hat{S}^2 that are between 0 and 2. For example, the level labeled by $l=0, f=2$, with the $f_a=1+f_b=1$ dissociation limit and an energy of -0.0106 cm^{-1} in Table I, has $\langle\hat{S}^2\rangle\approx 1.4$. On the other hand it has an expectation value of 2.1 for the operators \hat{f}_a^2 and \hat{f}_b^2 . As the latter value must lie between 2 and 6 the state can approximately be labeled with $f_a=1+f_b=1$. Notice, however, that this does not imply that the adiabatic approximation is valid. An expectation value $\langle\hat{f}_a^2\rangle=2.1$ only implies that most of the amplitude of the three-channel $l=0, f=2$ eigenfunction is in the atomic $|(f_a f_b)\rangle=|(11)\rangle$ state.

In the previous section the shapes of the $X^1\Sigma_g^+$ and $a^3\Sigma_u^+$ Born-Oppenheimer potentials have been optimized to reproduce all known levels with a binding energy of more than approximately 1 cm^{-1} . These BO potentials lead to close coupled predictions for the binding energy of the weakly bound levels that in several cases lie outside the error bars of the experiment. A final adjustment of the shape of the two BO potentials must be made. We chose to modify only the inner walls of both potentials. That is, we adjust only the B_i of the exponential form of Eq. (3). This adjustment does not significantly change the binding energies of the more deeply lying levels but leaves sufficient flexibility to obtain agreement between the experimental binding energies and those of the multichannel Hamiltonian. The best values for B_i are presented in Tables III and V. With these potentials the normalized standard deviation between the close coupling predictions and observations for 44 levels with a binding energy smaller than that of the singlet $v_X=62$ (present data and some from Ref. [8]) is $\sigma=0.63$ (normalized with the averaged experimental error), which shows the internal consistency of this approach.

V. MODELING OF EXPERIMENTAL LINE SHAPES

The spectra obtained in our beam experiment for the bound states of the Na dimer have been used to construct the $X^1\Sigma_g^+$ and $a^3\Sigma_u^+$ potentials. We have also observed spectra between the three f_a+f_b asymptotes. Figure 2 shows an example of a STIRAP spectrum that shows transitions to continuum states with odd partial waves. Figure 3 presents a spectrum with even partial waves using the $v'_A=139, J'_A=1$ rovibrational level of the $A^1\Sigma_u^+$ state as the intermediate in the Raman transition. The features between the three

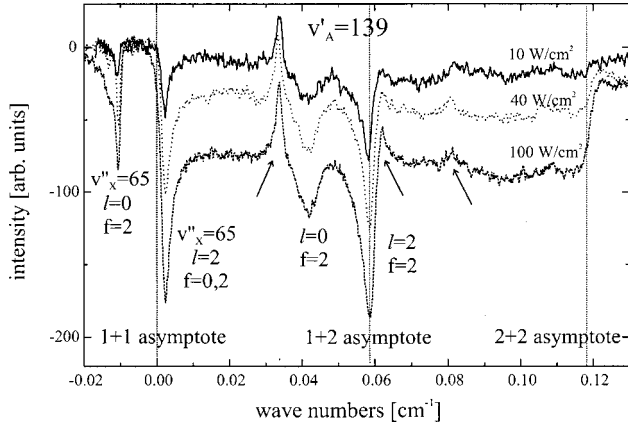


FIG. 3. Raman spectrum using the $v'_A = 139, J'_A = 1$ level of the $A \ ^1\Sigma_u^+$ state as the intermediate. Only even partial wave features are observable. The three curves correspond to three intensities of laser $L3$ and show the different saturation behavior of the resonances and the continuum (solid spectrum, $I_{L3} \approx 10 \text{ W/cm}^2$; dotted spectrum, $I_{L3} \approx 40 \text{ W/cm}^2$; dashed spectrum, $I_{L3} \approx 100 \text{ W/cm}^2$; $I_{L2} \approx 100 \text{ W/cm}^2$ for all spectra). Structures marked by arrows are $A-X$ transitions excited by $L3$ only. The zero of energy is at the $f_a = 1 + f_b = 1$ asymptote.

atomic hyperfine limits are significantly broader than those of bound states and can only be due to resonance phenomena in the continua.

In order to understand the broadening and to assign the resonances the Raman process is modeled theoretically. This should involve the two-photon transition from an initial rotational level J_X of the $X \ ^1\Sigma_g^+$ $v_X = 29$ vibrational state to a v'_A, J'_A rovibrational level of the A state and then to the continua of two colliding ground state Na atoms. For this paper we decided to model only the stimulated downward transition between the A state and the continua. That is, we assume that the first photon ($L2$) populates the unresolved hyperfine levels of the v'_A, J'_A A state equally. The ground state hyperfine structure for $v_X = 29$ is also unresolvable. This approximation ignores coherent two-photon processes. However, we believe that no additional features will appear from a more proper theory and that assignments of resonances and their widths are unaffected. The relative strength of the resonances is expected to be modified by a complete theoretical approach and therefore our modeled relative strengths must be treated with care. In addition, a sufficient signal-to-noise ratio in the experiment requires that the intensity of laser $L3$ must remain fairly high and consequently power broadening cannot be neglected. Again this will make the relative size of the features not directly comparable with a perturbative theoretical calculation.

The population model that is schematically drawn in Fig. 4 gives for the observed signal

$$I_q(\omega_3) \propto \sum_{\beta F' M'} \frac{\gamma_{\beta F'}}{2\pi} \int_0^\infty dE \times \sum_{\alpha FM} \frac{|\langle \alpha E^{(-)} FM | d_q | A \beta F' M' \rangle|^2}{(E + \hbar\omega_3 - E_{\beta F'})^2 + (\gamma_{\beta F'}/2)^2}, \quad (6)$$

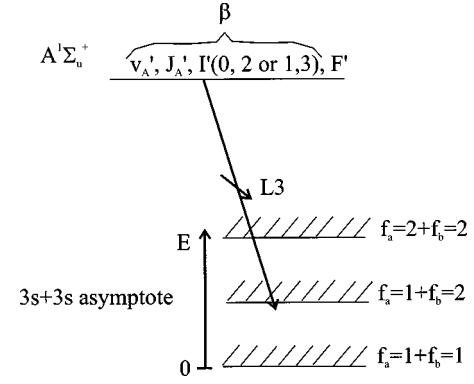


FIG. 4. Schematic of the population model where only one rovibrational level v'_A, J'_A of the A state is populated. It is assumed that the unresolved hyperfine levels labeled by total nuclear spin I' and the total spin $F' = J'_A + I'$ are equally populated. Laser $L3$ stimulates downward between the three ground state hyperfine asymptotes. The zero of energy is at the $f_a = 1 + f_b = 1$ asymptote.

where ω_3 is the laser frequency of the $L3$ laser and d_q the electronic dipole moment. The ket $|A \beta F' M'\rangle$ describes the wave function of the rovibrational A state level with energy $E_{\beta F'}$ and natural linewidth $\gamma_{\beta F'}$. The wave function is labeled by a total angular momentum \vec{F}' and β denotes the quantum numbers of the unresolved hyperfine structure. The ket $|\alpha E^{(-)} FM\rangle$ describes a multichannel scattering wave function with outgoing boundary conditions in spin channel $|\alpha FM\rangle$ and collision energy E . Here, $\alpha = (f_a f_b) fl$ and \vec{F} is the total angular momentum of the scattering wave function. The two summations run over all initial and final states where it is assumed that there is equal population of initial states $\beta F' M'$. The integration over collision energy describes a convolution of the energy-dependent square of the transition dipole moment and a Lorentzian with a width given by the natural lifetime.

The matrix element $\langle \dots | d_q | \dots \rangle$ is calculated in several steps ($q=0$ for linear polarization). First the vibrational wave function of the A state and the scattering wave function are evaluated. Subsequently, the two multichannel wave functions are combined to calculate the matrix element [3]. The excited state vibrational wave functions are obtained as in Ref. [18] and are calculated in a manner that is similar to that used here for the bound levels of the ground state Hamiltonian. The Hamiltonian that describes the interactions between 2S and 2P sodium, however, is more complex as the nonzero electronic angular momentum of the 2P atom introduces a far richer level structure. There are now eight Born-Oppenheimer potentials, spin-orbit interactions in addition to the rotational and hyperfine interactions. The positive energy or continuum multichannel wave functions of the ground state Hamiltonian are obtained using the renormalized Numerov propagator [19]. Outgoing boundary conditions in the atomic basis $|(f_a f_b) f l F\rangle$ are applied at large internuclear separations where the Born-Oppenheimer potentials are negligible compared to the collision energy. Scattering wave functions are labeled by their outgoing channel.

In the spectra two kinds of collisional resonance phenomena are observed. These are shape and Feshbach resonances.

The former occur only for nonzero partial waves and are due to nearly bound levels behind the centrifugal barrier. The scattering wave function inside this barrier is enhanced when the collision energy is near this resonance position, which implies that the transition moment can be enhanced as well, if the appropriate upper level is chosen. The width of the resonance is determined by tunneling through the centrifugal barrier.

Feshbach resonances are multichannel effects and occur only between the asymptotic states of the system [15]. For the Na dimer this occurs between the $f_a = 1 + f_b = 1$ and the $f_a = 2 + f_b = 2$ dissociation limits. The resonances are due to bound states of a subsystem of the full Hamiltonian that are weakly coupled to energetically open channels. This subsystem might be the adiabats that dissociate to the asymptotically closed states and then couple to a continuum by nonadiabatic mixing. Constructive or destructive interference near a Feshbach resonance can be observed in collisional cross sections or transition moments. In our case a direct transition from the excited rovibrational state to the outgoing $|(f_a f_b) f l F\rangle$ spin state interferes with an indirect process whereby first a transition to the resonance/bound state occurs and only then is the outgoing spin state accessed. The width of the resonance is determined by the coupling strength between the bound states of the subsystem and the outgoing continuum state and can give rise to asymmetric line profiles.

VI. INTERPRETATION OF THE OBSERVED SCATTERING RESONANCES

Figure 3 shows registrations with three different laser powers covering an energy range from below the $f_a = 1 + f_b = 1$ to above the $f_a = 2 + f_b = 2$ hyperfine asymptote. The intermediate level of the A state in the Raman transition is $v'_A = 139$, $J'_A = 1$. Therefore, the observed structures are due to resonances with $l = 0, 2$. The signals strongly depend on the intensity of $L3$, which varies from about $I_{L3} \approx 10$ W/cm² to $I_{L3} \approx 100$ W/cm². The three features marked by arrows are due to unwanted A - X transitions caused by laser $L3$ only. The figure shows the last bound state $v''_X = 65$, $l = 0$, $f = 2$ just below the lowest hyperfine asymptote and also an $l = 2$ shape resonance for $v''_X = 65$ which is just above the $f_a = 1 + f_b = 1$ threshold. Two additional resonances with large width compared to the bound state widths appear at higher frequencies.

Figure 3 also shows that with increasing power of $L3$ one observes that all resonance features grow in depth and broaden due to saturation.

The fluorescence level on the left side between $v''_X = 65$, $l = 0$, $f = 2$ and the $l = 2$, $f = 0, 2$ shape resonance is independent of the laser power of $L3$ and represents the ‘‘background’’ signal in the absence of two-photon transitions. Ignoring the dips caused by the resonances, the fluorescence level between the $f_a = 1 + f_b = 1$ and $f_a = 2 + f_b = 2$ hyperfine asymptotes is reduced relative to the background level. The reduction stems from direct transitions into the nonresonant continuum of the outgoing channels.

Figure 3 shows that the resonances saturate at lower laser intensities than that of the nonresonant continuum. A tenfold

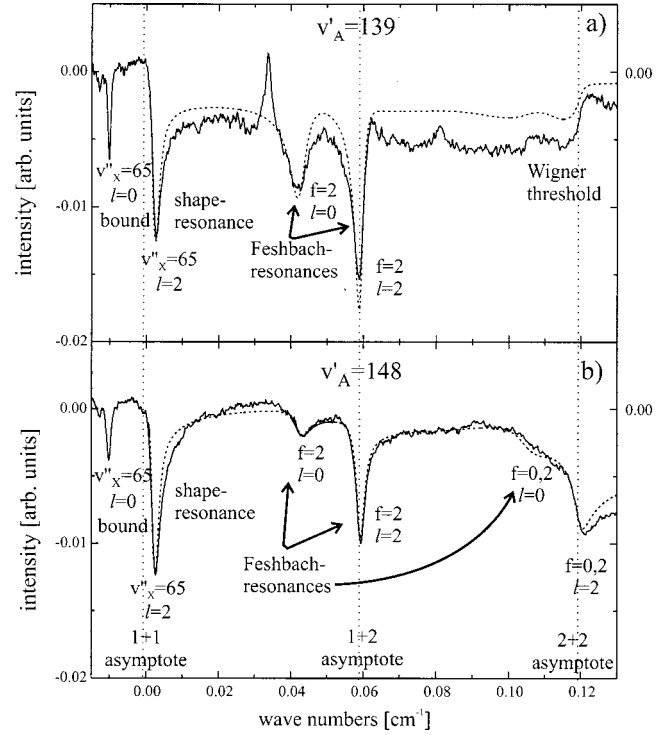


FIG. 5. Comparison of observed (solid) and simulated (dashed) spectra using different intermediate A $^1\Sigma_u^+$ state vibrational levels. The intermediate levels for panels (a) and (b) are $v'_A = 139$, $J'_A = 1$, and $v'_A = 148$, $J'_A = 1$, respectively. The zero of energy is at the $f_a = 1 + f_b = 1$ asymptote.

increase of the intensity increases the resonance dips by a factor of 3 while the nonresonant continuum increases by twice as much.

A comparison of the experimental and simulated line shapes is presented in Fig. 5. In panel (a) the solid line shows a spectrum with $v'_A = 139$, $J'_A = 1$ as intermediate level, and $I_{L3} \approx 40$ W/cm². This spectrum has already been shown in Fig. 3. Here it is overlaid with a theoretical profile (dashed line) calculated according to Eq. (6). The theoretical curve can reproduce almost all details of the experimental recording. The resonance positions agree within the experimental errors, typically 15 MHz. From an analysis of the simulated spectrum it follows that the sharp increase of fluorescence near the $f_a = 2 + f_b = 2$ hyperfine limit is a consequence of Wigner threshold effects in the scattering channels that open at this limit. Wigner threshold effects at the other two limits are obscured by the presence of a strong resonance.

The assignment of the resonances is obtained from a comparison with the simulation and the collision energy dependence E of the individual matrix elements $\langle \dots | d_q | \dots \rangle$. For example, we observe a shape resonance just above the lowest hyperfine asymptote. It is labeled by $v''_X = 65$, $l = 2$, and both $f = 0$ and 2. The two f components are not resolved as the resonance width 66 MHz is large compared to the splitting between the $f = 0$ and 2 lines. The resonance width is significantly larger than the 26 MHz experimental width that is determined from the linewidth of a true bound state. The Feshbach resonances at 0.04 cm⁻¹ and 0.06 cm⁻¹ are la-

beled by $f=2, l=0$, and $f=2, l=2$, respectively. Their asymmetry and full width at half maximum of 172 MHz and 99 MHz are in good agreement with the simulation. In Fig. 5 we show the spectra for $I \approx 40$ W/cm² laser intensity to enhance the structure of the weaker continuum signal. This results in some power broadening of the shape and Feshbach resonances. In the experimental scan of Fig. 5(a) the resonances are more saturated than the nonresonant continuum, explaining the difference in the background levels and the resonances depths for the observed and simulated continuum.

In panel (b) of Fig. 5 the STIRAP spectrum using the intermediate level $v'_A=148$ but the same $J'_A=1$ as in Fig. 5(a) and the corresponding simulation are shown. The intensity of $L3$ is 50 W/cm². The agreement between experiment and theory is remarkable despite the fact that the spectra of panels (a) and (b) are significantly different. For example, the frequency position and the form of the asymmetry of the $f=2, l=0$, and $f=2, l=2$ Feshbach resonances have changed. The simulation calculates a shift of $+0.00137$ cm⁻¹ for the $f=2, l=0$, resonance and -0.00057 cm⁻¹ for the $f=2, l=2$ Feshbach resonance if one uses $v'_A=148$ instead of $v'_A=139$. Moreover, additional resonances appear near the $f_a=2+f_b=2$ asymptote. The shoulder at 0.11 cm⁻¹ is due to two overlapping Feshbach resonances labeled $f=0, l=0$, and $f=2, l=0$, respectively, while the feature at the $f_a=2+f_b=2$ asymptote is due to $f=0, l=2$, and $f=2, l=2$ resonances.

The marked differences between panels (a) and (b) are due to the use of a different intermediate level. They differ in their outer turning point by about 9 \AA ($R_{139}=22 \text{ \AA}$ and $R_{148}=31 \text{ \AA}$). The matrix elements in Eq. (6) depend on the overlap between the excited state wave function and the multichannel scattering wave function. Consequently, by shifting the outer turning point of the excited state wave function the scattering wave function is sampled at different internuclear separations. This causes the relative contribution to the transition matrix element from the different channels of the multichannel scattering wave function to change. In the language of Feshbach theory, this is equivalent to a change of phase between and/or the relative size of the contribution from the embedded bound state and the outgoing scattering channel. This leads to modified line shapes and the appearance of additional lines. The shape resonance at the $f_a=1+f_b=1$ asymptote neither moves significantly nor changes its shape as there is no contribution from an outgoing scattering channel.

In addition to the low partial waves the experiment can also observe higher partial waves. Figure 6 shows a recording where $v'_A=148, J'_A=3$ was used as the upper level for the Raman scheme. The resulting structures are therefore due to d and g waves ($l=2,4$). The laser intensity is 50 W/cm². The g -wave resonances are significantly wider than the d -wave resonances. The agreement between the simulated and experimental spectra is again quite satisfactory and confirms the assignment of the resonances. The deviation of the intensity ratios is attributable to saturation of the sharp reso-

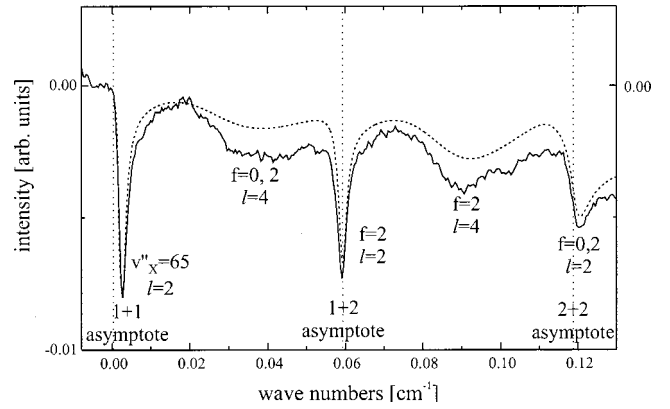


FIG. 6. Observed spectrum (solid) and simulation (dashed) using the $v'_A=148, J'_A=3$ level of the $A^1\Sigma_u^+$ state as the intermediate. Only d - and g -wave resonances are observable. The zero of energy is at the $f_a=1+f_b=1$ asymptote.

nances; thus the broad features appear stronger than expected.

The sudden increase of fluorescence near the $f_a=2+f_b=2$ asymptote [see Figs. 3 and 5(a)] can be used to precisely determine the dissociation limit. We find $D_0=5942.6879(41)$ cm⁻¹ (barycenter of hyperfine structure) which agrees with the earlier determination of $D_0=5942.6880(39)$ cm⁻¹ reported in [8,23].

The excellent agreement between the theoretical simulation and the observed spectra between the three hyperfine asymptotes clearly shows that we have an adequate model of the transition matrix elements as well as highly accurate Born-Oppenheimer potentials. The latter potentials not only predict the shape and Feshbach resonances between these atomic limits but also reproduce all bound state data available, as discussed in Secs. III and IV.

VII. DISCUSSION

A high resolution molecular beam experiment has been used to measure weakly bound levels below and resonance structures in the continuum between the Na_2 ground state asymptotes. The two-color experiment uses a STIRAP-like pulse sequence to transfer a specific deeply bound $X^1\Sigma_g^+$ rovibrational level into a near threshold dimer or a pair of scattering Na atoms. By properly choosing the initial rotational level the spectroscopic experiment is able to give detailed information about Na+Na collisional properties for a single partial wave.

With the spectroscopic information obtained in the current experiment and all data available in the literature, we have constructed precise $X^1\Sigma_g^+$ and $a^3\Sigma_u^+$ potentials which describe both states from their repulsive branch up to the outer turning points of asymptotic vibrational levels. For modeling the level structure of weakly bound states a coupled channel analysis based on these potentials has been used. Moreover, the resonance structures between the hyperfine asymptotes have been successfully simulated with a line shape model involving the transition dipole between the intermediate state of the STIRAP process and the coupled channel wave function of the scattering atoms. In this way

TABLE VI. Derived s -wave scattering lengths of Na+Na elastic collisions at various ground state hyperfine limits. The atomic states are labeled by atomic spin f_α and its magnetic projection m_{f_α} . The scattering length of the triplet potential equals that of the $f_a=2, m_{f_a}=2+f_b=2, m_{f_b}=2$ collision.

Asymptote	Scattering length		
f_a, f_b	m_{f_a}	m_{f_b}	$[a_0]$
1,1	1(-1)	1(-1)	52.98(40)
	1(-1)	0(0)	52.98(40)
	1	-1	49.23(40)
	0	0	51.12(40)
2,2	2(-2)	2(-2)	62.51(50)
singlet potential			19.20(30)

shape and Feshbach resonances have been assigned. Thus the potentials can be used to describe the continuum up to the highest hyperfine asymptote.

We can now use the accurate Born-Oppenheimer potentials to derive scattering lengths for ultracold collisions between two Na atoms. The results are given in Table VI. The uncertainties shown in the table are estimated by systematically varying the potential branch at short internuclear separations over a range that gives still a consistent description of the set of measured bound states. They should cover the range of 1σ . We believe that the main source of uncertainty is the uncertainties in the $a^3\Sigma_u^+$ potential rather than those in the $X^1\Sigma_g^+$ potential. Systematic corrections and additional uncertainties due to effects not included in the ground state Hamiltonian, such as hyperfine parameters that depend on internuclear separation, cannot be ruled out.

Our scattering lengths for $f_a=1+f_b=1$ collisions are at the edge of the error bars of the scattering lengths presented in Ref. [4], in which the accuracy is probably overestimated because the dependence of the scattering length on the nodal positions of the wave function [Eq. (8) in [4]] is very steep for the nodes used in the evaluation.

Our results for the shape of the Born-Oppenheimer potentials and scattering lengths can be compared with other recent determinations. Ho *et al.* [5] constructed potentials using spectroscopic data that do not include the three most weakly bound vibrational levels of the Born-Oppenheimer potentials. Consequently, their long range shape of the potentials is less reliable. Additionally, the equilibrium internuclear separation of the triplet potential derived in that work $R_e=5.089(62)$ Å is slightly different from our value $5.1665(95)$ Å, which included the rotational energy obtained in the study of the transition $1^3\Sigma_g^+ \leftarrow a^3\Sigma_u^+$ by Färbert and Demtröder [13].

Van Abeelen and Verhaar [6] extracted scattering lengths using the same spectroscopic data as in Ref. [5] and, more crucially, using data from the study of magnetic-field-induced Feshbach resonances in ultracold Na+Na collisions [7] in order to more carefully represent the long range region of the potentials. Their singlet scattering length $[a_s=19.1(21)a_0]$ and our value agree to within the quoted uncertainties. However, for the triplet there is a 3σ discrepancy [Ref. [6], $a_t=65.3(9)a_0$].

We have tried to investigate the origin of the discrepancy between our and van Abeelen and Verhaar's triplet scattering length. Reference [6] uses slightly different dispersion coefficients and a different shape of the exchange interaction. Replacing our long range parameters with those of Ref. [6] and reanalyzing all our data results in a potential with a slightly larger standard deviation of $\sigma=0.76$. The standard deviation with the potential presented in Tables III, IV, and V is $\sigma=0.63$. The scattering lengths for this analysis are $0.4a_0$ larger than those of our initial evaluation. The small increase of the triplet scattering length is insufficient to explain the 3σ discrepancy between the value of Ref. [6] and our value presented in Table VI.

A recent paper on Feshbach resonances in a time-dependent magnetic field [15] contains as a by-product another set of scattering lengths ($a_s=20.3a_0$, $a_t=63.9a_0$). These scattering lengths were chosen to reproduce the Feshbach resonances of Ref. [7]. Nevertheless, the deviations from our values indicate the scatter between the currently existing evaluations of the scattering lengths.

None of the analysis above includes retardation effects. These are expected from calculations by Marinescu *et al.* [24] to be less than 0.4% for internuclear separations smaller than 100 Å and are already within the error limits of the dispersion coefficients. Thus, with the presently achieved experimental accuracy, it will be difficult to distinguish between $1/R^6$ or $1/R^7$ behavior at the asymptote.

In the current experiment no external magnetic field is present and consequently the Born-Oppenheimer potentials are based on zero magnetic field data. A logical extension of our work is to combine these data with the observation of Feshbach resonances in a magnetic field [7] and thereby improve the Born-Oppenheimer potentials. Advances can also be expected by adding an external magnetic field to the current Raman experiment. We will report on these experiments in the near future [25]. As the experiments refine the measurements of the near threshold bound state, the current close coupled modeling of these states might be insufficient and effects of internuclear-separation-dependent hyperfine constants might become apparent.

Finally, manipulation of asymptotic levels and scattering processes by near resonant laser light [26] can also lead to a better knowledge of the interaction potentials between atoms. First successful steps in this direction have already been taken in our laboratory. The influence of near resonant light fields on vibrational levels near the A state asymptote was observed in a molecular beam experiment. The extension of this experiment to studies at the ground state asymptote seems to be more difficult; the number of spatially overlapping lasers increases and thus the signal will be more sensitive to the laser field distribution in the resonance volume. This will lead to problems in specifying the involved Rabi frequencies.

ACKNOWLEDGMENTS

This work was supported by the Deutsche Forschungsgemeinschaft within the SFB 407. E. Tiesinga thanks the Army Research Office and the Office of Naval Research of the United States of America for support.

- [1] *Bose-Einstein Condensation*, special issue of J. Res. Natl. Inst. Stand. Technol. **101** (1996).
- [2] F. Dalfovo, S. Giorgini, and L. P. Pitaevskii, Rev. Mod. Phys. **71**, 463 (1999); *Bose-Einstein Condensation in Atomic Gases*, Proceedings of the International School of Physics “Enrico Fermi,” Course 140, edited by M. Inguscio (IOS, Amsterdam, 1999).
- [3] E. Tiesinga, C. J. Williams, P. S. Julienne, K. M. Jones, P. D. Lett, and W. D. Phillips, J. Res. Natl. Inst. Stand. Technol. **101**, 505 (1996).
- [4] A. Crubellier, O. Dulieu, F. Masnou-Seeuws, M. Elbs, H. Knöckel, and E. Tiemann, Eur. Phys. J. D **6**, 211 (1999).
- [5] T. S. Ho, H. Rabitz, and G. Scoles, J. Chem. Phys. **112**, 6218 (2000).
- [6] F. A. van Abeelen and B. J. Verhaar, Phys. Rev. A **59**, 578 (1999).
- [7] S. Inouye, M. R. Andrews, J. Stenger, H.-J. Miesner, D. M. Stamper-Kurn, and W. Ketterle, Nature (London) **392**, 151 (1998).
- [8] M. Elbs, H. Knöckel, T. Laue, C. Samuelis, and E. Tiemann, Phys. Rev. A **59**, 3665 (1999).
- [9] U. Gaubatz, P. Rudecki, S. Schieman, and K. Bergmann, J. Chem. Phys. **92**, 5363 (1990).
- [10] P. Kusch and M. M. Hessel, J. Chem. Phys. **68**, 2591 (1978).
- [11] R. F. Barrow, J. Verges, C. Effantin, K. Hussein, and J. D’Incan, Chem. Phys. Lett. **104**, 179 (1984).
- [12] L. Li, S. F. Rice, and R. W. Field, J. Chem. Phys. **82**, 1178 (1985).
- [13] A. Färbert and W. Demtröder, Chem. Phys. Lett. **264**, 225 (1997).
- [14] H. T. C. Stoof, J. M. V. A. Koelman, and B. J. Verhaar, Phys. Rev. B **38**, 4688 (1988).
- [15] F. H. Mies, E. Tiesinga, and P. S. Julienne, Phys. Rev. A **61**, 022721 (2000).
- [16] G. Audi and A. H. Wapstra, Nucl. Phys. A **595**, 409 (1995).
- [17] E. Arimondo, M. Inguscio, and P. Violini, Rev. Mod. Phys. **49**, 31 (1977).
- [18] E. Tiesinga, C. J. Williams, and P. S. Julienne, Phys. Rev. A **57**, 4257 (1998).
- [19] B. R. Johnson, J. Chem. Phys. **67**, 4086 (1977).
- [20] P. Kharchenko, J. F. Babb, and A. Dalgarno, Phys. Rev. A **55**, 3566 (1997).
- [21] M. Marinescu, H. R. Sadeghpour, and A. Dalgarno, Phys. Rev. A **49**, 982 (1994).
- [22] G. Hadinger, G. Hadinger, S. Magnier, and M. Aubert-Frécon, J. Mol. Spectrosc. **175**, 441 (1996).
- [23] K. M. Jones, S. Maleki, S. Bize, P. D. Lett, C. J. Williams, H. Richling, H. Knöckel, E. Tiemann, H. Wang, P. L. Gould, and W. C. Stwalley, Phys. Rev. A **54**, R1006 (1996).
- [24] M. Marinescu, J. F. Babb, and A. Dalgarno, Phys. Rev. A **50**, 3096 (1994).
- [25] T. Laue, E. Tiesinga, C. Samuelis, H. Knöckel, and E. Tiemann (unpublished).
- [26] P. O. Fedichev, Y. Kagan, G. V. Shlyapnikov, and J. T. M. Walraven, Phys. Rev. Lett. **77**, 2913 (1996).